Selective CO₂ reduction electrocatalysis using AgCu nanoalloys prepared by a "host-guest" method

Marta Śliwa^{†,^}, Hao Zhang^{‡,^}, Jiaxin Gao[‡], Benjamin O. Stephens[†], Andrew J. Patera[†],

Anthony Shoji Hall^{‡,*}, and Thomas J. Kempa^{†,‡,*}

- † Department of Chemistry, Johns Hopkins University, Baltimore, MD
- ‡ Department of Materials Science and Engineering, Johns Hopkins University, Baltimore, MD
- ^ These authors contributed equally to this work
- * Corresponding authors

Keywords: host-guest synthesis, nanoparticles, alloys, electrocatalysis, CO₂ reduction reaction, faradaic efficiency

Abstract:

Multi-metallic nanoalloys have attracted considerable interest as catalysts in a number of electrochemically-driven reactions, because their tunable surface structure and composition offers a route towards enhancing the efficiency and selectivity of many chemical processes. However, the preparation of homogeneous bimetallic alloy nanoparticles remains a challenge. Here, we present a room-temperature and scalable, host-guest approach for synthesis of dilute Cu in Ag alloy nanoparticles. In this approach, an ionic silver bromide precursor harbors exogenous Cu cations which are then co-reduced alongside interstitial Ag cations to yield nanoparticles (15–30 nm in diameter) comprised of a AgCu alloy. Facile alteration of the synthesis protocol allows one to tune the % Cu loading within the AgCu nanoparticles, while maintaining the crystal structure and plasmonic features. AgCu nanoparticles with a 5% nominal loading of Cu exhibit peak activity (–0.23 mA/cm² surface area normalized partial current density) and selectivity (83.2% faradaic efficiency) for CO product formation from electrocatalytic reduction of CO2 at relatively mild

overpotentials. Moreover, given a modest mass loading of 0.20 mg/cm², our AgCu nanoalloy has a higher mass activity compared to literature reports of Ag- and Cu-containing nanomaterials used for similar electrocatalytic transformations. Our host-guest synthesis platform may be extended to a range of other multi-metallic nanoalloys with relevance to electrocatalysis and optics.

Main Text

Synthetic tuning of nanoparticle (NP) size, shape, and composition is central to the effective use of such materials in optoelectronic^{1,2,3,4}, medical^{5,6,7,8}, and energy applications. Out of the broad family of NP architectures reported to date, multi-component NPs^{9,10,11,12}, such as bimetallic and alloy NPs, have attracted interest because their properties can be engineered to reflect a hybridization or synergistic interaction between their component elements.¹³ Such synergies are especially sought after in electrocatalytic applications, where the mixing of component materials can give rise to reactive sites that catalyze new reaction pathways or known pathways that are commonly difficult to activate. In bimetallic NPs, improvements to the efficiency and selectivity of electrocatalytic processes can be realized through precise control over catalytic site ensembles, 14 electronic structure tunability, ^{15,16} and increased stability. ¹⁴ Examples include methanol oxidation reaction catalysis with Pt–Ru catalysts, 15 ethanol oxidation over Pt–Pd NPs, 16 CO oxidation using Au–Ag alloy NPs, ¹⁷ and oxygen reduction performed over Au–Pt catalysts, ¹⁸ among many others. In some instances, the incorporation of more expensive, electrocatalytically active materials such as Au, Ag, and Pt as the dilute element within a parent matrix of more abundant transition metals can lead to reduced catalyst material cost, but without sacrifice of overall catalytic performance.

The catalytic performance of alloy nanoparticles is highly sensitive to their composition, and therefore synthetic methods capable of finely regulating the concentration of any given element within the NP alloy is of paramount importance. Existing strategies for the preparation of nanoscale alloys include co-reduction methods, ¹⁹ seed-mediated or two-step growth, ²⁰ galvanic replacement, ²¹ the use of ionic-liquid systems, ²² or thermal decomposition techniques. ²³ Many fundamental parameters, including precursor redox potential, nanoparticle lattice structure, atomic radii and melting points, ²⁴ dictate whether the aforementioned approaches can successfully yield a desired alloy phase. It is often the case that an interplay of these parameters simply results in phase segregation of the component elements (e.g., if miscibility limits are exceeded), thereby limiting the applicability of these approaches. Other approaches, such as "one pot" laser ablation²⁵ and electrodeposition²⁶ techniques, use higher energies to force thermodynamic alloy products, and are limited in their ability to yield morphologically well-defined, uniform nanostructures with high product yields.

Increased interest in de-carbonizing the chemical industry motivates the development of new catalyst formulations, including nanoparticle alloys with atom-precise compositions. Of the many chemical processes of industrial relevance, the electrochemical reduction of carbon dioxide has received extensive attention over the last few decades as it could be used to convert the potent greenhouse gas into feedstock chemicals. Within this context, Cu NPs have been identified as promising catalysts for the CO₂ reduction reaction (CO₂RR) primarily due to the optimal binding of the *CO intermediate^{27,28} on the Cu NP surface, which in turn affords increased selectivity for C₂ and C_n reaction products. However, some limitations must be overcome. First, the catalytic activity of Cu nanoparticles is hindered by their high susceptibility to oxidation upon exposure to air.^{29,30} Second, although binary phase diagrams indicate that Cu and Ag are immiscible,³¹ they share a common crystal structure (fcc), accessible valence state (+1), and an approximate 15% difference in atomic radii, thereby satisfying three of four Hume-Rothery rules for metallic alloy

formation.^{32,33} Given these criteria, preparing bimetallic NPs with Cu as the dilute species in Ag appears to be a realistic target, especially if new synthetic approaches can mitigate the immiscibility problem. Third, while a diverse array of Ag- and Cu-containing materials have been realized, the high-temperature reductions, multi-step seeded growth routes, or electrodeposition approaches commonly used to prepare bimetallic Ag–Cu foams,³⁴ aerogels,³⁵ and nanoparticles^{26,37,38} often yield materials with phase segregated components and some of these methods may not be well suited for industrial scale-up. Techniques do exist for forming more precise and homogenous Ag–Cu alloy NPs, but many use dense solvents and bulky ligand-based polyol methods,³⁹ less convenient air-free thermal decomposition techniques,⁴⁰ or non-equilibrium rapid thermal shock treatments.⁴¹ Finally, increasing interest in the production of syngas or CO from CO₂ has drawn attention to Ag-based catalysts. Therefore, there is a clear need for simple, scalable, and versatile synthetic methods for the preparation of Ag–Cu alloys that are phase pure and compositionally tunable.

In this work, we present a new "host-guest" synthesis route for the preparation of phase-pure "Cu in Ag" alloy nanoparticles (AgCu NPs) and explore their performance in the electrocatalytic reduction of CO₂. We adapted our previously reported synthesis protocols⁴² to prepare AgCu alloy nanoparticles with a controllable Cu composition for 0% (Cu free), 2.5%, 5%, 7.5%, 10% and 15% nominal Cu loadings. As shown in **Figure 1a**, the first synthetic step in the process (I) is the formation of a silver-copper-bromide Ag(Cu^{x+})Br nanoparticle—hereafter the *host* particle. Exogenous copper cations are introduced during the synthesis of the AgBr host particle, which serves to localize the precursors for the synthesis of the alloy product. At the next stage (II) interstitial silver and copper cation *guests* harbored in the silver halide *host* lattice are co-reduced via mild solution-phase processes: addition of a 1 M solution of *L*-Arginine to a solution containing

the Ag(Cu^{x+})Br particles followed by irradiation with 254 nm ultraviolet (UV) light leads to the precipitation of a single metallic phase on the parent Ag(Cu^{x+})Br particle surface to form AgCu|AgBr dimers. Finally, the AgBr phase is selectively digested to yield the target AgCu NPs (III).

To characterize the size and morphology of AgCu alloy NPs (Figure S1) prepared through our host-guest chemical synthesis, we used bright-field transmission electron microscopy (TEM) to image samples with 0 - 15% nominal Cu loadings. Analyses of TEM data collected on a 5% Cu sample reveal spherical nanoparticles with a narrow size distribution and an average diameter of 21 ± 3 nm (Figure 1b). We also investigated particle morphology at three key stages of the synthesis. First, the average sizes of the Ag(Cu^{x+})Br host particles are comparable and unchanged across the 0–15% Cu range with mean diameters of $18-20 \pm 2$ nm (Figure S2). We do not expect these particles to experience significant strain from inclusion of Cu ions, because these species occupy interstitial sites within the AgBr lattice. Interestingly, host particles with lower % Cu undergo more rapid reduction under electron irradiation during TEM imaging than do host particles with higher Cu loadings. This more rapid reduction manifests in the more rapid nucleation and growth of the AgCu phase during observation under the TEM, and this trend holds even for host particles already subjected to solution-phase reduction with L-Arginine (Figure S3a-b). Second, following solution-phase reduction, the AgCu phases of dimer particles prepared from host particles with Cu loadings of 0, 2.5, 5 7.5, 10, and 15% Cu exhibit average diameters of $20 \pm$ 3.5 nm, 17 ± 2.5 nm, 17 ± 3 nm, 16 ± 2.5 nm, 16 ± 2.7 and 16 ± 2.7 nm, respectively (**Figure S3**). Third, after etching of the dimers, the liberated AgCu NPs prepared from host particles loaded with 0, 2.5, 7.5, 10, and 15% Cu reveal average diameters of 33 ± 5 nm, 27 ± 5 nm, 21 ± 3 nm, 19 ± 4 nm, and 16 ± 2 nm, respectively (Figure S4). The AgCu NPs post-etch (Figure S4) are

larger than their AgCu phase counterpart in the dimer (**Figure S3**) likely due to continued growth and ripening of the NPs during the 12 hour solution etching process. The monotonic decrease in average size and oblateness of the AgCu NPs with increasing Cu loading may be attributed to the increase in lattice strain (the atomic radii of Ag and Cu differ by ~15%) that accompanies increasing concentrations of Cu, yielding smaller and rounder particles.

UV-visible absorption spectroscopy was used to probe the optical properties of products generated at all key stages of the synthesis. Irradiation of the Ag(Cu^{x+})Br host particles with UV light in the presence of *L*-Arginine yields a purple solution whose absorption spectrum features peaks centered at 370 nm and 550 nm (**Figure 1c**). These peaks are not present in a solution containing the host particles before irradiation and are similar to those that we have previously ascribed⁴² to dimers comprised of Ag NPs fused to their AgBr host phase. The narrow feature at 370 nm and the broad feature centered at roughly 550 nm may stem from two distinct resonances excited within the AgCu phase of the dimer that originate from the anisotropic dielectric environment around this phase: part of the AgCu is covered by ligands and solvent molecules while the remainder forms a heterointerface with the AgBr host particle. Subsequent etching of the AgBr component of the dimer yields a yellow solution whose absorption spectrum is characterized by a single peak centered at 405 nm. This peak falls within the characteristic surface plasmon resonance band for Ag nanoparticles ($\lambda = 360-410$ nm),^{43,44} and is in keeping with the expected nominal shift^{45,46,47} of the Ag plasmon resonance with Cu doping.

The aforementioned spectral features were also examined at each of the six Cu loadings mentioned above. The two peaks characteristic of the dimer and the one peak diagnostic of the AgCu NP show no significant variation over the range of six copper compositions (**Figure 1c** inset; **Figure S5 – S6**). Likewise, all absorption peaks are well preserved upon a 10-fold increase

in reagent volume (**Figure S7**), thus indicating the scalability of our synthetic approach. With regards to the AgCu NPs, increased loading of Cu results in attenuation of the broad absorption tail > 500 nm. This observation may be explained by the formation of more spherical NPs at higher % Cu loadings (**Figure S3 – S4**) whose surface plasmon bands should appear symmetric like those well documented for Ag NPs. The foregoing analyses reveal a retention of clear plasmonic signatures, which are independent of Cu loading up to 15%, band suggest that these nanoparticle alloys could hold promise in photocatalytic applications.

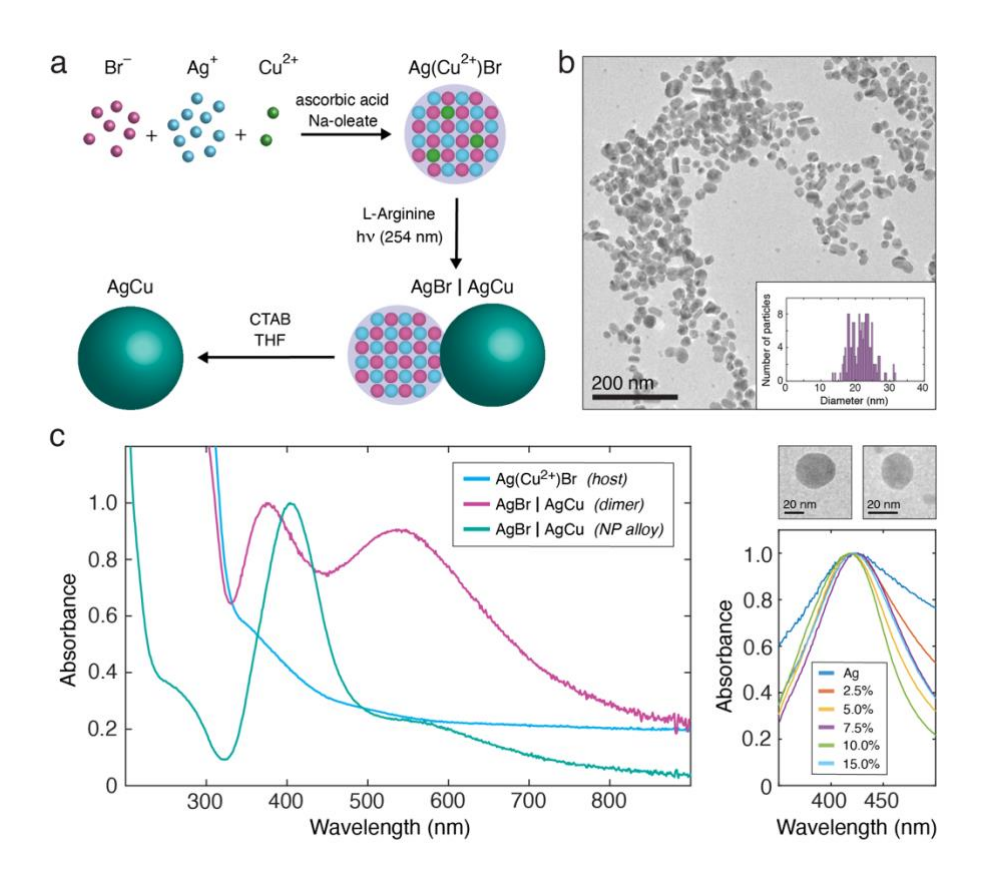


Figure 1: (a) Scheme describing key steps of the solution phase synthesis of AgCu NPs. (b) Bright-field TEM image of AgCu NPs with 5% Cu loading; Inset: Histogram of NP size. (c) Left: Absorption spectra of AgBr nanoparticles (blue trace, normalized to peak maximum at 374 nm), AgCu | AgBr dimers (purple trace, normalized to maximum at 374 nm), and 5% AgCu NPs (teal trace, normalized to maximum at 405 nm). Right: Normalized absorption spectra of AgCu NPs

containing the indicated % Cu loadings focusing on the peak centered at ~408 nm. TEM images from left to right are of individual AgCu NPs with 0% and 5% Cu loadings, respectively.

A detailed assessment of the structure and composition of the AgCu alloy NPs was carried out using high magnification TEM and fast-Fourier transform (FFT) analysis of individual particles across the aforementioned Cu composition range. FFT-derived diffractograms from the lattice of AgCu NPs with 0%, 5%, 10%, and 15% Cu loading each exhibit spots that are consistent with scattering from an fcc lattice (Figure 2a and Figure S8). These data suggest that Cu incorporation does not appear to distort significantly the cubic Ag lattice and that the AgCu materials retain crystallographic order over the range of Cu loadings tested. Next, the elemental composition of the AgCu NPs was characterized by energy dispersive X-ray spectroscopy (EDS) to identify the actual Cu loading into the particles. EDS composition maps (Figure 2b and Figure S9) for AgCu NPs with 2.5%, 5%, and 7.5% nominal Cu loading clearly reflect the presence of both Ag and Cu in the particles. Analyses of EDS line scans acquired across AgCu NPs at the different Cu loadings (Figure S10 – S11) reveal a consistent spatial distribution of Ag and Cu suggesting that the Cu is uniformly distributed throughout the particle (ie., the Cu does not appear to segregate forming islands or a shell) up to 7.5% nominal loading. Average d-spacing values for the 0%, 2.5%, 5%, 7.5%, 10% and 15% AgCu NPs are comparable to the Ag(111) d-spacing value of 0.2325 nm (Figure 2c).⁴⁸ With an increase in % Cu loading, a slight decrease in the mean value of the dspacing is observed, though this trend is not statistically significant as it lies within the errors of our analysis of the TEM images. Collectively, these EDS and TEM data indicate the presence of small and uniformly distributed quantities of Cu in the Ag lattice at a level that avoids significant disruption of the lattice parameters. To perform a semi-quantitative analysis of the Cu composition in the AgCu alloy NPs, we integrated the X-ray counts associated with the $L\alpha = 0.93$ keV, $K\alpha =$

8.04 keV, and $K\beta = 8.91$ keV⁴⁹ Cu lines (**Figure 2d**). These EDS analyses and elemental concentrations determined by inductively coupled plasma mass spectrometry provide evidence for a steady increase in % Cu content up to 7.5% nominal loading (**Table S2 – S3** and **Figure S12**). Therefore, we conclude that straightforward introduction of varying concentrations of Cu^{2+} during preparation of the metal-halide host is sufficient for tuning the percent Cu composition in the final AgCu NP.

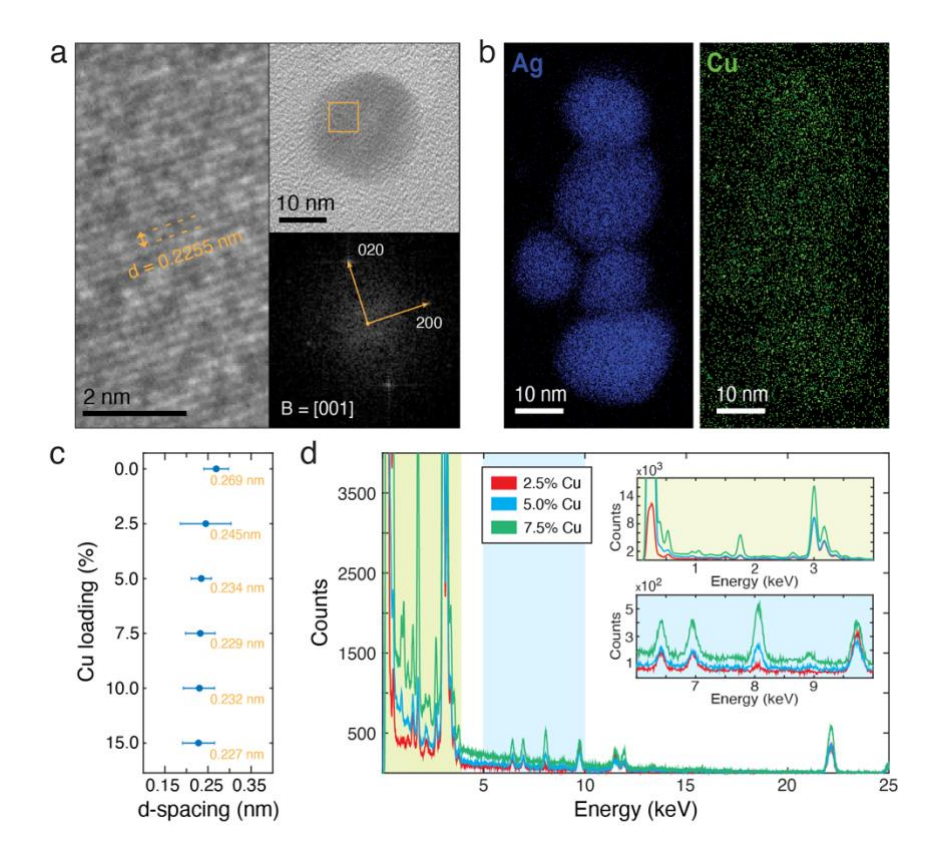


Figure 2: (a) Bright-field TEM image of a AgCu NP with 5% Cu loading and corresponding lattice image taken at high magnification. Inset: Indexed FFT-derived diffractogram acquired from the region outlined by the orange square in the TEM image above. (b) EDS maps of Ag and Cu content in a cluster of 5% Cu AgCu NPs. (c) Average d-spacing values (exact values in orange) for AgCu NPs across the Cu loading range. Bars denote one standard deviation. (d) EDS spectra of AgCu NPs with 2.5% (red trace), 5% (blue trace) and 7.5% (green trace) Cu loading. Light green inset reveals spectra within the 0–4 keV region that contain the Ag Lα peak (2.984 keV) and Cu Lα

peak (0.93 keV). Light blue inset reveals spectra within the 6–10 keV region that contain the Cu K α peak (8.04 keV) and the Cu K β peak (8.91 keV).

Having established that our host-guest approach yields alloyed AgCu NPs whose composition can be tuned, we evaluated the activity and selectivity of these materials towards the electrocatalytic reduction of CO₂. The AgCu NPs were formulated as nanoparticle inks and then sprayed onto a gas diffusion layer to form a gas diffusion electrode (Figure S13). Gas and liquidphase reaction products were analyzed using gas chromatography-mass spectroscopy (GCMS) and nuclear magnetic resonance spectroscopy (NMR), respectively. The faradaic efficiency (FE), which is a measure of the efficiency with which electrons participate in a given electrochemical transformation, was obtained for each of the AgCu NPs at 0%, 2.5%, 5%, 7.5%, 10%, and 15% nominal Cu loading at -0.5 V_{RHE} (Figure 3a). The FEs were calculated by finding the ratio of experimentally detected gaseous product(s) to the theoretical yields based on the observed current density (Supporting Information, Materials and Methods). The major product from AgCu NP catalysis of the CO₂ reduction reaction (CO₂RR) was CO, and the product with the second highest yield was H₂. Only trace amounts of formate and acetate (FE_{Formate} and FE_{Acetate} at < 1% of sampled product) were detected as liquid-phase products (Figure S14). Samples containing AgCu NPs with a 5% nominal Cu loading exhibited the highest FEco, namely, up to 85%. A three-fold increase in targeted Cu loading (15%) resulted in a decrease in FEco to 50%. The specific activity of the AgCu NP electrodes was assessed by measuring the electrochemically active surface area (ECSA)normalized total current density, jecsa. The electrochemical surface area of each AgCu NP loaded electrode was determined through the lead underpotential deposition (UPD) method (Figure S15 and Table S4). Similar to the FE_{CO} trend, an increase in Cu loading from 0 to 5% resulted in an

increase in j_{ECSA} from -0.2 to -0.3 mA/cm² at -0.5V_{RHE}, with a significant decrease to -0.14 mA/cm² at 15% Cu loading.

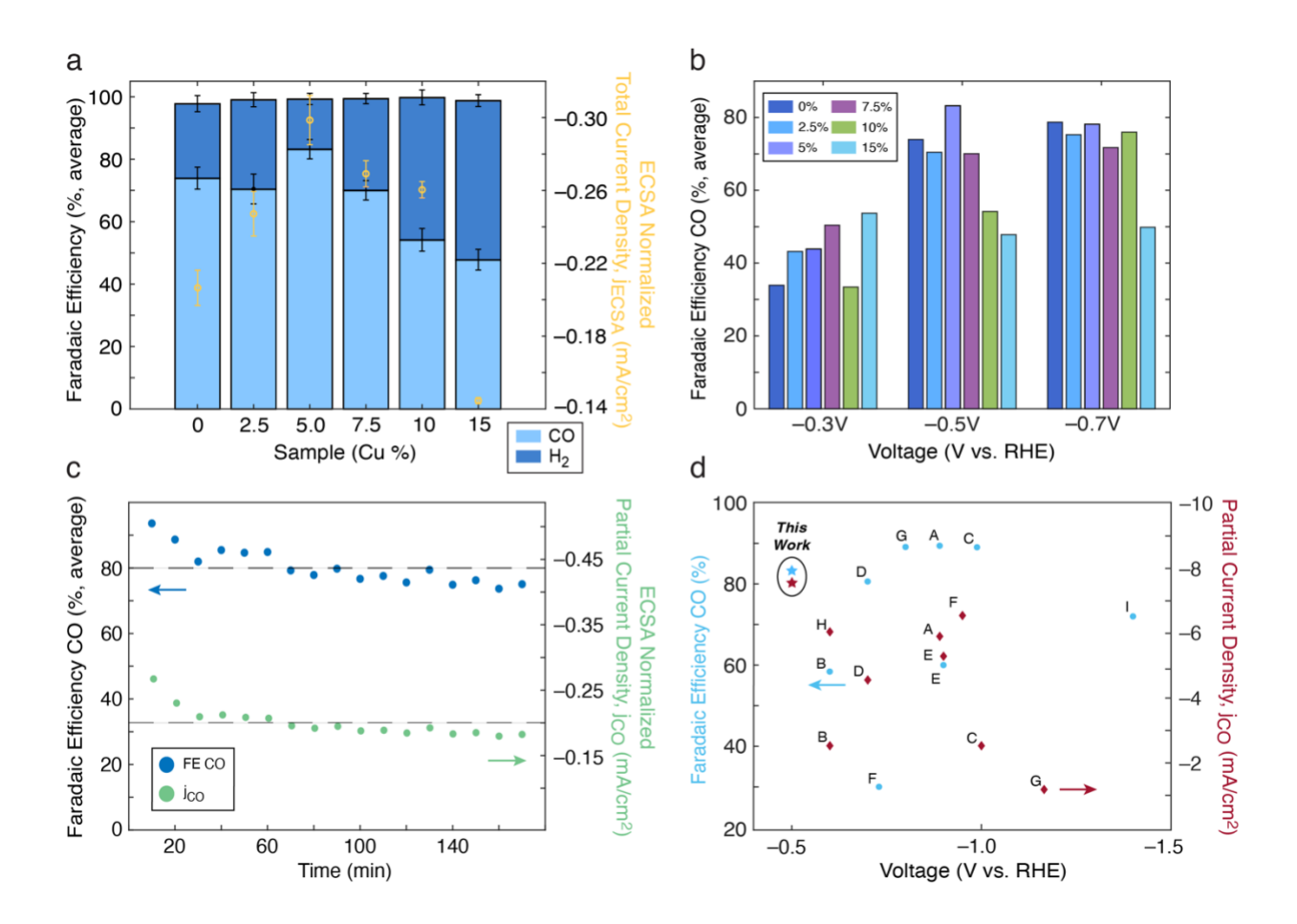


Figure 3: Data collected during the electrochemical CO₂ reduction reaction on a gas diffusion electrode loaded with AgCu NPs containing different Cu loadings. (a) Faradaic efficiencies of CO (FEco) and H₂ (FE_{H2}) product for samples with various % Cu loadings, at an overpotential of − 0.5V_{RHE}. The 5% Cu loading sample exhibits the highest FE_{CO} and highest suppression of H₂ products. An overlay of the ECSA normalized total current density plot (yellow markers) is also included. The current was normalized by the electrochemical active surface area of the sample (see Figure S15, Table S4). (b) FEco at −0.3V_{RHE}, −0.5 V_{RHE} and −0.7 V_{RHE} for all samples in the compositional range. The 5% Cu sample exhibits a maximum in catalytic selectivity. (c) Results from stability assessment of a 5% AgCu NP electrode performed over a 180 min period at −0.5 V_{RHE}. FE_{CO} and ECSA normalized partial current density *j*_{co} data were collected at 10 min intervals. (d) Comparison of the FE_{CO} and geometric partial current density *j*_{co} of this work

(denoted by stars) to published Ag/Cu bimetallic material systems used as catalysts in the CO₂RR (A–I). Competitive selectivity and reaction efficiency are achieved by our nanoalloy at relatively mild overpotentials relative to prior work (**Table S5**).

To further assess the catalytic performance of the AgCu NP electrodes, the electrocatalyzed CO₂RR was performed on samples at each of the six Cu loading levels at overpotentials of –0.3, –0.5, and –0.7 V_{RHE} (**Figure 3b**). At a relatively low overpotential of –0.3 V_{RHE}, all samples yield a lower FE_{CO} than at higher (more negative) overpotentials of –0.5 and –0.7 V_{RHE} (**Figure S16**). Hydrogen production from the catalysis of the competing hydrogen evolution reaction is more prevalent at the low overpotential of –0.3 V_{RHE} and from electrodes containing AgCu NPs with > 10% Cu loading. At –0.5 V_{RHE}, a clear maximum in CO selectivity is seen for the 5% Cu electrode with an average FE_{CO} value of 83.23%. More negative overpotentials of –0.7 V_{RHE} yielded FE_{CO} values that stayed relatively constant for the 0% – 10% Cu electrodes, with a decrease to 50% FE at 15% Cu loading. We attribute the overall reduction in performance of the 15% Cu electrode to possible formation of Cu-rich phases (as Cu solubility limit in Ag is exceeded, see **Table S3**) which exhibit high activity for hydrogen evolution reaction catalysis.

Based on measured FE_{CO}, j_{ECSA} and j_{CO} values, the 5% AgCu NP loaded electrode is the highest performing CO₂RR catalyst in our material series. The stability of the 5% AgCu NP was assessed by measuring the FE_{CO} and ECSA-normalized j_{CO} of the sample over a 180 min period at -0.5 V_{RHE} (**Figure 3c** and **Figure S17**). A 14% decrease in FE_{CO} across the 180 min sampling period, and a decrease in ECSA-normalized j_{CO} from -0.25mA/cm² to -0.18mA/cm², indicate that the NP catalysts did not undergo appreciable damage or decrease in activity during the stability measurements. Scanning electron microscopy (SEM) imaging of the electrodes before and after

the 180 min stability assessment revealed no apparent surface reconstruction or visible material loss (**Figure S18**).

The activity and selectivity of the AgCu NPs synthesized in this work were compared to various literature examples of Ag/Cu bimetallic materials used as catalysts for the CO₂RR (**Figure 3d**). With an FE of 83.23% and j_{CO} of 7.52 mA/cm², our 5% Cu in Ag nanoalloy is comparably selective at much less negative overpotentials to and more than three times more active than Cu@Ag core-shell nanoparticles (ref. C in **Figure 3d** and **Table S5**), and also performs well compared to other Ag/Cu containing nanostructures. Moreover, our material yields these values at modest overpotentials and at mass loadings of 0.2 mg/cm², which are approximately 2–5 times lower than a majority of the highlighted examples. Our AgCu nanoalloy catalyst platform also offers structural advantages. High material porosity, such as that exhibited by the bimetallic foams, ^{34,50} aerogels, ³⁵ and sponge-like ⁵¹ systems included in our comparison, is closely associated with catalytic activity. When deposited on the electrode surface, our AgCu NPs not only form a highly active, porous network, but also retain their individual structural integrity. The latter feature aids in establishing clear structure-catalytic property relationships which can be difficult to assess within large-network foam or gel systems wherein particle sintering and network loss is common.

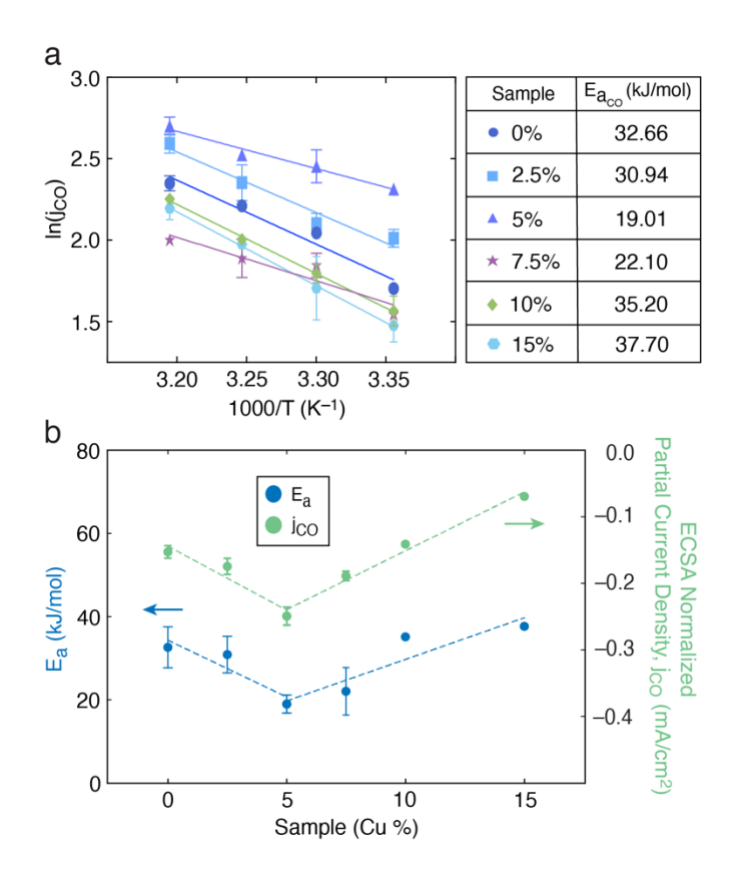


Figure 4: (a) Arrhenius plot of temperature dependent activity of the –15% AgCu NP catalysts as CO₂ reduction is performed (at -0.5 V_{RHE} in 1 M KOH) on a gas diffusion electrode. Table: summary of E_a values (kJ/mol) calculated from the slope of each sample line. (b) Overlay of the activation energy for CO production and ECSA normalized partial current density j_{CO} for the 0–15% AgCu NP samples.

To better understand the mechanism of CO₂ reduction on our AgCu NPs, we performed CO₂RR experiments across a range of temperatures at a fixed potential of –0.5 V_{RHE}. As temperature was increased from 25 to 40 °C a systematic increase in FE_{CO} was observed for each AgCu NP sample (**Figure S19**). These CO₂RR experiments were used to furnish an Arrhenius plot of partial current density of CO (j_{CO}) as function of the inverse of absolute temperature for each of the 0–15% AgCu NP samples. The activation energy for the formation of CO (extracted from the slope of the Arrhenius plot) initially decreases as a function of increasing Cu loading, with the 5%

AgCu NP samples exhibiting the lowest E_a of 19.01 kJ/mol. As Cu loading increases beyond 5%, there is a monotonic increase in the activation energy to 37.69 kJ/mol. This trend indicates that CO production is highly sensitive to the amount of Cu loading within the AgCu nanoalloys and that the 5% AgCu NP sample presents the lowest energy barrier for CO formation. Moreover, this trend coincides with the trend of CO activity (jco) for all AgCu particles. It is likely that the lower activation energy for CO formation exhibited by the 5% AgCu NP sample stems from lower adsorption barrier of the CO intermediate via electronic effects between Ag and Cu, which are intimately coupled at the solubility limit of this nanoalloy.⁵²

Conclusion

We have synthesized dilute Cu in Ag alloy nanoparticles (AgCu NPs) through an unique solution-phase "host-guest" method. The Cu content within the AgCu nanoalloy products can be tuned with retention of crystal structure and plasmonic signatures of the Ag majority component. Electrodes loaded with AgCu NPs containing 5% Cu exhibit the highest activity and selectivity for CO formation during electrocatalytic reduction of CO₂. The 5% AgCu NP catalyst also exhibited the lowest activation energy for the CO product out of the series of AgCu NP compositions tested, a result we attribute to the lower adsorption barrier for the CO intermediate on the alloyed Ag-Cu surface. Our work provides a versatile host-guest synthetic platform for preparation of a range of alloyed nanoparticles and other complex multicomponent materials with applications in optoelectronics and electrocatalysis, among others.

ASSOCIATED CONTENT

Supporting Information

The Supporting Information is available free of charge. Contents:

Supplementary Materials and Methods containing the following: (1) detailed nanoparticle catalyst synthesis protocols, (2) sample preparation and characterization, (3) electrocatalysis protocols, and (4) electrochemical analyses.

Supplementary Figures S1–S19 and Tables S1–S6 containing the following: (1) size distributions of nanoparticles at key stages of synthesis, (2) UV-vis spectra of nanoparticles at key stages of synthesis, (3) TEM images and associated diffractograms, (4) EDS maps and line scans, (5) ICPMS data, (6) electrochemical data and analyses (e.g., cyclic voltammograms, UPD analyses, results of CO₂RR at various temperatures), (7) NMR of liquid products, (8) description of quantification of gas products via gas diffusion electrode, (9) SEM images of AgCu NPs before and after electrocatalysis, and (10) quantitative data tables (e.g., mass loadings, EDS data, ICPMS analyses, ECSA analysis, literature comparisons, and electrode calibration data).

AUTHOR INFORMATION

Corresponding Author

Thomas J. Kempa – Department of Chemistry and Department of Materials Science and Engineering, Johns Hopkins University, Baltimore, Maryland 21218, United States; ORCID: 0000-0002-1672-8325 *Email:* tkempa@jhu.edu

Anthony S. Hall – Department of Materials Science and Engineering, Johns Hopkins University, Baltimore, Maryland 21218, United States; *Email:* shoji@jhu.edu

Author Contributions

M.S., A.S.H., and T.J.K. designed the study. M.S. and H.Z. performed all experiments with input from T.J.K. and A.S.H. All authors contributed to data analyses. The manuscript was written with contributions from all authors. All authors have approved the final version of the manuscript. ^: Authors contributed equally.

Funding Sources

T.J.K. acknowledges funding from a National Science Foundation (DMR-1848046) CAREER grant which supported characterization studies in this work. A.S.H. acknowledges funding from a National Science Foundation (CHE-02102648) which supported this work.

ABBREVIATIONS

CO₂RR: carbon-dioxide reduction reaction

FE: faradaic efficiency

TEM: transmission electron microscopy

BF: bright-field

UV-Vis: UV-Visible spectroscopy

EDS: energy dispersive x-ray spectroscopy

FFT: fast-Fourier transform

SEM : scanning electron microscopy

UPD: underpotential deposition

References

- (1) Chiang, I.-C.; Chen, D.-H. Synthesis of Monodisperse FeAu Nanoparticles with Tunable Magnetic and Optical Properties. *Advanced Functional Materials* **2007**, *17* (8), 1311–1316. https://doi.org/10.1002/adfm.200600525.
- (2) Scarabelli, L.; Coronado-Puchau, M.; Giner-Casares, J. J.; Langer, J.; Liz-Marzán, L. M. Monodisperse Gold Nanotriangles: Size Control, Large-Scale Self-Assembly, and Performance in Surface-Enhanced Raman Scattering. ACS Nano 2014, 8 (6), 5833–5842. https://doi.org/10.1021/nn500727w.
- (3) Juodėnas, M.; Tamulevičius, T.; Henzie, J.; Erts, D.; Tamulevičius, S. Surface Lattice Resonances in Self-Assembled Arrays of Monodisperse Ag Cuboctahedra. *ACS Nano* 2019, 13 (8), 9038–9047. https://doi.org/10.1021/acsnano.9b03191.
- (4) Xing, L.; Xiahou, Y.; Zhang, P.; Du, W.; Xia, H. Size Control Synthesis of Monodisperse, Quasi-Spherical Silver Nanoparticles To Realize Surface-Enhanced Raman Scattering Uniformity and Reproducibility. ACS Appl. Mater. Interfaces 2019, 11 (19), 17637–17646. https://doi.org/10.1021/acsami.9b02052.
- (5) Grancharov, S. G.; Zeng, H.; Sun, S.; Wang, S. X.; O'Brien, S.; Murray, C. B.; Kirtley, J. R.; Held, G. A. Bio-Functionalization of Monodisperse Magnetic Nanoparticles and Their Use as Biomolecular Labels in a Magnetic Tunnel Junction Based Sensor. *J. Phys. Chem. B* 2005, 109 (26), 13030–13035. https://doi.org/10.1021/jp051098c.
- (6) Tang, L.; Fan, T. M.; Borst, L. B.; Cheng, J. Synthesis and Biological Response of Size-Specific, Monodisperse Drug–Silica Nanoconjugates. *ACS Nano* **2012**, *6* (5), 3954–3966. https://doi.org/10.1021/nn300149c.
- (7) Shen, L.; Bao, J.; Wang, D.; Wang, Y.; Chen, Z.; Ren, L.; Zhou, X.; Ke, X.; Chen, M.; Yang, A. One-Step Synthesis of Monodisperse, Water-Soluble Ultra-Small Fe3O4

- Nanoparticles for Potential Bio-Application. *Nanoscale* **2013**, *5* (5), 2133–2141. https://doi.org/10.1039/C2NR33840H.
- (8) Si, P.; Yuan, E.; Liba, O.; Winetraub, Y.; Yousefi, S.; SoRelle, E. D.; Yecies, D. W.; Dutta, R.; de la Zerda, A. Gold Nanoprisms as Optical Coherence Tomography Contrast Agents in the Second Near-Infrared Window for Enhanced Angiography in Live Animals. ACS Nano 2018, 12 (12), 11986–11994. https://doi.org/10.1021/acsnano.8b03862.
- (9) Park, G.; Seo, D.; Jung, J.; Ryu, S.; Song, H. Shape Evolution and Gram-Scale Synthesis of Gold@Silver Core—Shell Nanopolyhedrons. *J. Phys. Chem. C* **2011**, *115* (19), 9417–9423. https://doi.org/10.1021/jp200338p.
- (10) Jukk, K.; Kongi, N.; Tammeveski, K.; Solla-Gullón, J.; Feliu, J. M. PdPt Alloy Nanocubes as Electrocatalysts for Oxygen Reduction Reaction in Acid Media. *Electrochemistry Communications* 2015, 56, 11–15. https://doi.org/10.1016/j.elecom.2015.04.001.
- (11) Gao, C.; Hu, Y.; Wang, M.; Chi, M.; Yin, Y. Fully Alloyed Ag/Au Nanospheres:

 Combining the Plasmonic Property of Ag with the Stability of Au. *J. Am. Chem. Soc.* **2014**, *136* (20), 7474–7479. https://doi.org/10.1021/ja502890c.
- (12) Chen, J.; Feng, J.; Yang, F.; Aleisa, R.; Zhang, Q.; Yin, Y. Space-Confined Seeded Growth of Cu Nanorods with Strong Surface Plasmon Resonance for Photothermal Actuation. *Angewandte Chemie* 2019, *131* (27), 9376–9382. https://doi.org/10.1002/ange.201904828.

- (13) Srinoi, P.; Chen, Y.-T.; Vittur, V.; Marquez, M. D.; Lee, T. R. Bimetallic Nanoparticles: Enhanced Magnetic and Optical Properties for Emerging Biological Applications. *Applied Sciences* **2018**, *8* (7), 1106. https://doi.org/10.3390/app8071106.
- (14) García-Diéguez, M.; Finocchio, E.; Larrubia, M. Á.; Alemany, L. J.; Busca, G. Characterization of Alumina-Supported Pt, Ni and PtNi Alloy Catalysts for the Dry Reforming of Methane. *Journal of Catalysis* 2010, 274 (1), 11–20. https://doi.org/10.1016/j.jcat.2010.05.020.
- (15) Lin, M.-L.; Lo, M.-Y.; Mou, C.-Y. PtRuP Nanoparticles Supported on Mesoporous

 Carbon Thin Film as Highly Active Anode Materials for Direct Methanol Fuel Cell.

 Catalysis Today 2011, 160 (1), 109–115. https://doi.org/10.1016/j.cattod.2010.05.018.
- (16) Hou, S.; Xu, Y.; Liu, Y.; Xu, R.; Zhang, B. Room-Temperature Fast Synthesis of Composition-Adjustable Pt–Pd Alloy Sub-10-Nm Nanoparticle Networks with Improved Electrocatalytic Activities. *Chem. Lett.* **2012**, *41* (5), 546–548. https://doi.org/10.1246/cl.2012.546.
- (17) Liu, J.-H.; Wang, A.-Q.; Chi, Y.-S.; Lin, H.-P.; Mou, C.-Y. Synergistic Effect in an Au–Ag Alloy Nanocatalyst: CO Oxidation. *J. Phys. Chem. B* **2005**, *109* (1), 40–43. https://doi.org/10.1021/jp044938g.
- (18) Luo, J.; Njoki, P. N.; Lin, Y.; Wang, L.; Zhong, C. J. Activity-Composition Correlation of AuPt Alloy Nanoparticle Catalysts in Electrocatalytic Reduction of Oxygen.
 Electrochemistry Communications 2006, 8 (4), 581–587.
 https://doi.org/10.1016/j.elecom.2006.02.001.
- (19) Cai, S.; Qi, C.; Li, Y.; Han, Q.; Yang, R.; Wang, C. PtCo Bimetallic Nanoparticles with High Oxidase-like Catalytic Activity and Their Applications for Magnetic-Enhanced

- Colorimetric Biosensing. *J. Mater. Chem. B* **2016**, *4* (10), 1869–1877. https://doi.org/10.1039/C5TB02052B.
- (20) Li, H.; Wu, H.; Zhai, Y.; Xu, X.; Jin, Y. Synthesis of Monodisperse Plasmonic Au Core–Pt Shell Concave Nanocubes with Superior Catalytic and Electrocatalytic Activity. *ACS Catal.* **2013**, *3* (9), 2045–2051. https://doi.org/10.1021/cs400223g.
- (21) Sun, X.; Yang, Y.; Zhang, Z.; Qin, D. Mechanistic Roles of Hydroxide in Controlling the Deposition of Gold on Colloidal Silver Nanocrystals. *Chem. Mater.* 2017, 29 (9), 4014–4021. https://doi.org/10.1021/acs.chemmater.7b00575.
- (22) Akiyoshi, K.; Watanabe, Y.; Kameyama, T.; Kawawaki, T.; Negishi, Y.; Kuwabata, S.; Torimoto, T. Composition Control of Alloy Nanoparticles Consisting of Bulk-Immiscible Au and Rh Metals via an Ionic Liquid/Metal Sputtering Technique for Improving Their Electrocatalytic Activity. *Phys. Chem. Chem. Phys.* 2022, 24 (39), 24335–24344. https://doi.org/10.1039/D2CP01461K.
- (23) Vasquez, Y.; Luo, Z.; Schaak, R. E. Low-Temperature Solution Synthesis of the Non-Equilibrium Ordered Intermetallic Compounds Au3Fe, Au3Co, and Au3Ni as Nanocrystals. *J. Am. Chem. Soc.* **2008**, *130* (36), 11866–11867. https://doi.org/10.1021/ja804858u.
- (24) Thota, S.; Wang, Y.; Zhao, J. Colloidal Au–Cu Alloy Nanoparticles: Synthesis, Optical Properties and Applications. *Mater. Chem. Front.* **2018**, *2* (6), 1074–1089. https://doi.org/10.1039/C7QM00538E.
- (25) Amendola, V.; Meneghetti, M.; Bakr, O. M.; Riello, P.; Polizzi, S.; Anjum, D. H.; Fiameni, S.; Arosio, P.; Orlando, T.; Fernandez, C. de J.; Pineider, F.; Sangregorio, C.;

- Lascialfari, A. Coexistence of Plasmonic and Magnetic Properties in Au89Fe11
 Nanoalloys. *Nanoscale* **2013**, *5* (12), 5611–5619. https://doi.org/10.1039/C3NR01119D.
- (26) Hoang, T. T. H.; Verma, S.; Sichao Ma; Fister, T. T.; Timoshenko, J.; Frenkel, A. I.; Kenis, P. J. A.; Gewirth, A. A. Nanoporous Copper–Silver Alloys by Additive–Controlled Electrodeposition for the Selective Electroreduction of CO2 to Ethylene and Ethanol. *J. Am. Chem. Soc.* 2018, 140 (17), 5791–5797. https://doi.org/10.1021/jacs.8b01868.
- (27) Peterson, A. A.; Abild-Pedersen, F.; Studt, F.; Rossmeisl, J.; Nørskov, J. K. How Copper Catalyzes the Electroreduction of Carbon Dioxide into Hydrocarbon Fuels. *Energy Environ. Sci.* **2010**, *3* (9), 1311–1315. https://doi.org/10.1039/C0EE00071J.
- (28) Nie, X.; Esopi, M. R.; Janik, M. J.; Asthagiri, A. Selectivity of CO2 Reduction on Copper Electrodes: The Role of the Kinetics of Elementary Steps. *Angewandte Chemie* **2013**, *125* (9), 2519–2522. https://doi.org/10.1002/ange.201208320.
- (29) Rice, K. P.; Walker, E. J. Jr.; Stoykovich, M. P.; Saunders, A. E. Solvent-Dependent Surface Plasmon Response and Oxidation of Copper Nanocrystals. *J. Phys. Chem. C* **2011**, *115* (5), 1793–1799. https://doi.org/10.1021/jp110483z.
- (30) Chan, G. H.; Zhao, J.; Hicks, E. M.; Schatz, G. C.; Van Duyne, R. P. Plasmonic
 Properties of Copper Nanoparticles Fabricated by Nanosphere Lithography. *Nano Lett.*2007, 7 (7), 1947–1952. https://doi.org/10.1021/nl070648a.
- (31) *Desk Handbook: Phase Diagrams for Binary Alloys*, 2nd ed.; Okamoto, H., Ed.; ASM International: Materials Park, Ohio, 2010.
- (32) Miyajima, K.; Fukushima, N.; Himeno, H.; Yamada, A.; Mafuné, F. Breakdown of the Hume–Rothery Rules in Sub-Nanometer-Sized Ta-Containing Bimetallic Small

- Clusters. *J. Phys. Chem. A* **2009**, *113* (48), 13448–13450. https://doi.org/10.1021/jp908415y.
- (33) Miyajima, K.; Himeno, H.; Yamada, A.; Yamamoto, H.; Mafuné, F. Nanoalloy

 Formation of Ta-Containing Trimetallic Small Clusters. *J. Phys. Chem. A* **2011**, *115* (9),

 1516–1520. https://doi.org/10.1021/jp1095932.
- (34) Kottakkat, T.; Klingan, K.; Jiang, S.; Jovanov, Z. P.; Davies, V. H.; El-Nagar, G. A. M.; Dau, H.; Roth, C. Electrodeposited AgCu Foam Catalysts for Enhanced Reduction of CO2 to CO. *ACS Appl. Mater. Interfaces* **2019**, *11* (16), 14734–14744. https://doi.org/10.1021/acsami.8b22071.
- (35) Wang, W.; Gong, S.; Liu, J.; Ge, Y.; Wang, J.; Lv, X. Ag-Cu Aerogel for Electrochemical CO2 Conversion to CO. *Journal of Colloid and Interface Science* **2021**, 595, 159–167. https://doi.org/10.1016/j.jcis.2021.03.120.
- (36) Huang, J.; Mensi, M.; Oveisi, E.; Mantella, V.; Buonsanti, R. Structural Sensitivities in Bimetallic Catalysts for Electrochemical CO2 Reduction Revealed by Ag–Cu Nanodimers. *J. Am. Chem. Soc.* 2019, *141* (6), 2490–2499. https://doi.org/10.1021/jacs.8b12381.
- (37) Freire, R. M.; Rojas-Nunez, J.; Elias-Arriaga, A. L.; Fujisawa, K.; Troncoso, L.; Denardin, J. C.; Baltazar, S. E. Natural Arrangement of AgCu Bimetallic Nanostructures through Oleylamine Reduction. *Inorg. Chem. Front.* **2020**, *7* (24), 4902–4912. https://doi.org/10.1039/D0QI00940G.
- (38) Chang, Z.; Huo, S.; Zhang, W.; Fang, J.; Wang, H. The Tunable and Highly Selective Reduction Products on Ag@Cu Bimetallic Catalysts Toward CO2 Electrochemical

- Reduction Reaction. *J. Phys. Chem. C* **2017**, *121* (21), 11368–11379. https://doi.org/10.1021/acs.jpcc.7b01586.
- (39) Rahman, L.; Qureshi, R.; Yasinzai, M. M.; Shah, A. Synthesis and Spectroscopic Characterization of Ag-Cu Alloy Nanoparticles Prepared in Various Ratios. *Comptes Rendus Chimie* **2012**, *15* (6), 533–538. https://doi.org/10.1016/j.crci.2012.03.012.
- (40) Dou, Q.; Li, Y.; Wong, K. W.; Ng, K. M. Facile Synthesis of Nearly Monodisperse AgCu Alloy Nanoparticles with Synergistic Effect against Oxidation and Electromigration. *Journal of Materials Research* **2019**, *34* (12), 2095–2104. https://doi.org/10.1557/jmr.2019.71.
- (41) Yang, C.; Ko, B. H.; Hwang, S.; Liu, Z.; Yao, Y.; Luc, W.; Cui, M.; Malkani, A. S.; Li, T.; Wang, X.; Dai, J.; Xu, B.; Wang, G.; Su, D.; Jiao, F.; Hu, L. Overcoming Immiscibility toward Bimetallic Catalyst Library. *Science Advances* 2020, 6 (17), eaaz6844. https://doi.org/10.1126/sciadv.aaz6844.
- (42) Kossak, A. E.; Stephens, B. O.; Tian, Y.; Liu, P.; Chen, M.; Kempa, T. J. Anisotropic and Multicomponent Nanostructures by Controlled Symmetry Breaking of Metal Halide Intermediates. *Nano Lett.* 2018, *18* (4), 2324–2328. https://doi.org/10.1021/acs.nanolett.7b05090.
- (43) Halas, N. J.; Lal, S.; Chang, W.-S.; Link, S.; Nordlander, P. Plasmons in Strongly Coupled Metallic Nanostructures. *Chem. Rev.* 2011, 111 (6), 3913–3961. https://doi.org/10.1021/cr200061k.
- (44) Lee, J.; Hasan, W.; Stender, C. L.; Odom, T. W. Pyramids: A Platform for Designing Multifunctional Plasmonic Particles. *Acc. Chem. Res.* 2008, 41 (12), 1762–1771. https://doi.org/10.1021/ar800126p.

- (45) Chowdhury, S.; Bhethanabotla, V. R.; Sen, R. Effect of Ag–Cu Alloy Nanoparticle Composition on Luminescence Enhancement/Quenching. *J. Phys. Chem. C* 2009, *113* (30), 13016–13022. https://doi.org/10.1021/jp900294z.
- (46) Zhou, M.; Wang, Z.; Sun, Q.; Wang, J.; Zhang, C.; Chen, D.; Li, X. High-Performance Ag–Cu Nanoalloy Catalyst for the Selective Catalytic Oxidation of Ammonia. *ACS Appl. Mater. Interfaces* **2019**, *11* (50), 46875–46885.

 https://doi.org/10.1021/acsami.9b16349.
- (47) Rahman, L.; Shah, A.; Lunsford, S. K.; Han, C.; Nadagouda, M. N.; Sahle-Demessie, E.; Qureshi, R.; Khan, M. S.; Kraatz, H.-B.; Dionysiou, D. D. Monitoring of 2-Butanone Using a Ag–Cu Bimetallic Alloy Nanoscale Electrochemical Sensor. *RSC Adv.* **2015**, *5* (55), 44427–44434. https://doi.org/10.1039/C5RA03633J.
- (48) Chen, R.; Nuhfer, N. T.; Moussa, L.; Morris, H. R.; Whitmore, P. M. Silver Sulfide Nanoparticle Assembly Obtained by Reacting an Assembled Silver Nanoparticle Template with Hydrogen Sulfide Gas. *Nanotechnology* 2008, *19* (45), 455604. https://doi.org/10.1088/0957-4484/19/45/455604.
- (49) Krause, M. O.; Oliver, J. H. Natural Widths of Atomic K and L Levels, Kα X-ray Lines and Several KLL Auger Lines. *Journal of Physical and Chemical Reference Data* 1979, 8 (2), 329–338. https://doi.org/10.1063/1.555595.
- (50) Lee, H.; Kim, S.-K.; Ahn, S. H. Electrochemical Preparation of Ag/Cu and Au/Cu Foams for Electrochemical Conversion of CO2 to CO. *Journal of Industrial and Engineering Chemistry* **2017**, *54*, 218–225. https://doi.org/10.1016/j.jiec.2017.05.036.
- (51) Zhang, W.; Xu, C.; Hu, Y.; Yang, S.; Ma, L.; Wang, L.; Zhao, P.; Wang, C.; Ma, J.; Jin,
 Z. Electronic and Geometric Structure Engineering of Bicontinuous Porous Ag–Cu

- Nanoarchitectures for Realizing Selectivity-Tunable Electrochemical CO2 Reduction.

 Nano Energy 2020, 73, 104796. https://doi.org/10.1016/j.nanoen.2020.104796.
- (52) Clark, E. L.; Hahn, C.; Jaramillo, T. F.; Bell, A. T. Electrochemical CO2 Reduction over Compressively Strained CuAg Surface Alloys with Enhanced Multi-Carbon Oxygenate Selectivity. *J. Am. Chem. Soc.* 2017, *139* (44), 15848–15857. https://doi.org/10.1021/jacs.7b08607.